Physics of Fluids

RESEARCH ARTICLE | FEBRUARY 08 2023

Characterization and predictive modeling of a trajectory-oriented dual-mode scramjet combustor

Ruixu Zhou (周芮旭) ; Tuo Li (李拓) ; Xinyang Li (李心阳) ; Huan Lian (连欢)

Physics of Fluids 35, 026108 (2023)
https://doi.org/10.1063/5.0136170

Physics of Fluids ARTICLE scitation.org/journal/phf

Characterization and predictive modeling of a trajectory-oriented dual-mode scramjet combustor

Cite as: Phys. Fluids **35**, 026108 (2023); doi: 10.1063/5.0136170
Submitted: 24 November 2022 · Accepted: 17 January 2023 ·
Published Online: 8 February 2023

Ruixu Zhou (周芮旭),[1,2] Tuo Li (李拓),[1,2] Xinyang Li (李心阳),[1,2] and Huan Lian (连欢)[2,a)]

AFFILIATIONS

[1]School of Engineering Science, University of Chinese Academy of Sciences, Beijing 100049, China
[2]State Key Laboratory of High Temperature Gas Dynamics, Institute of Mechanics, Chinese Academy of Sciences, Beijing 100190, China

[a)]Author to whom correspondence should be addressed: hlian@imech.edu.cn

ABSTRACT

Linear and nonlinear characteristics of a dual-mode scramjet combustor are investigated in ground-simulated acceleration and deceleration trajectory experiments. The experiments were conducted in the direct-connected transient flight trajectory simulator 1 at the Institute of Mechanics, Chinese Academy of Sciences. High-frequency pressure measurements, the schlieren, and CH^* chemiluminescence high-speed imaging were applied for the diagnostics. Based on the quantitative analysis, the physical processes of acceleration and deceleration in general represent similar nonlinear characteristics. The linear characteristics are limited to the low-frequency oscillation period in the presence of physical governing mechanisms. A nonlinear predictive model of the dual-mode scramjet combustor based on historical measurements is proposed due to its generality for the acceleration and deceleration trajectory.

I. INTRODUCTION

Dual-mode scramjet (DMSJ) is one of the key enabling technologies for high-speed vehicles.[1] The complex nature of the internal reactive flow characteristics coupled with mechanisms of chemical reactions, fuel injection and dispersion, ignition and turbulent combustion, etc.,[2] results in a highly nonlinear system and causes challenges for engine control, especially online control. Therefore, it is important to quantify and understand the nonlinear system behavior that is essential to predict the short-term future of the engine performance and enable online control.

For linear quantification and prediction, the fast Fourier transform (FFT) is usually adopted. Based on the FFT and the linear decomposition method of proper orthogonal decomposition (POD), the dynamic mode decomposition (DMD), which is an approximation of the nonlinear Koopman spectral analysis,[3,4] has been developed by Schmid[5,6] to extract the linear dynamic modes from the time series data.[7–9] Combining the time coefficient and growth rate of each mode, the future parameter prediction can be achieved based on the DMD linear superposition.

For nonlinear quantification and prediction, a more systematic scheme of the nonlinear time series (NLTS) analysis has been developed over the decades to quantify and understand the time invariants. The phase space is constructed based on the scheme that reveals more information about the nonlinear dynamics of the time series data. The NLTS analysis has been applied by various researchers to evaluate the nonlinear characteristics of the reactive flow dynamics of both the premixed and diffusion flame.[10,11] For instance, Lorenz proposed "Method of Analogues" in 1969.[12] More recently, Domen *et al.*[13] and Gotoda *et al.*[14] proposed to use the multi-scale entropy as a method of online monitor to prevent the lean blowout in a laboratory-scale gas turbine model combustor. In addition, the Method of Analogues prediction method has been applied with good accuracy. Other approaches for the reactive flow prediction have been focused on the data-driven method of machine learning.[15–18] More recently, Deng *et al.*[19] adopted a dual-path flow reconstruction model based on the deep learning method and predicted the flow field in the combustor. Gaudron *et al.*[18] adopted four types of machine learning algorithms to predict the thermo-acoustic instabilities. Kong *et al.*[20,21] successfully reconstructed the velocity field in the isolator from the wall pressure measurements and achieved short-term prediction of the flame profile. However, the deep learning method requires a huge amount of reliable data as training inputs, which limits its online applications.

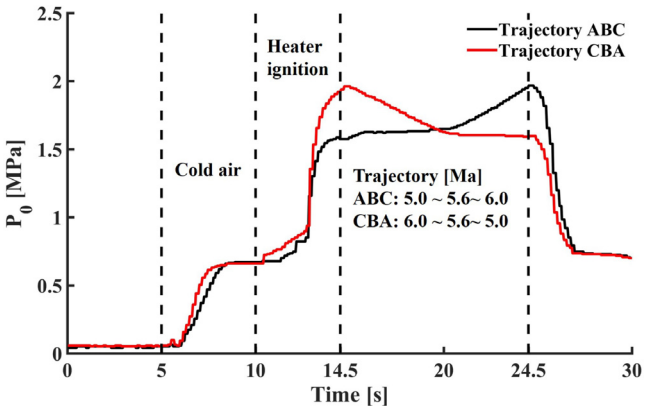

FIG. 1. Total pressure of the transient operation heater for trajectories ABC and CBA.

The flight trajectory designed with fixed dynamic pressure reduces the possibility of optimized flight trajectory and limits the flight envelope. Thus, the ability of transient trajectory design with varying total pressure, temperature, dynamic pressure, and the flight Mach number is a key enabling technology for the next generation flight vehicles. The nature of compressible fluid mechanics is the distorted continuity in space and time, thus, the quasi-steady analysis based on space and time continuity would not be sufficient for the design of transient flight trajectories. Despite the comprehensive study of the steady-state performance of the dual-mode scramjet combustor covering aspects of the fuel mixing, ignition, and combustion stabilization, studies on the transient combustion behavior are sparse in the literature due to the absence of transient operation facility and tremendously high computational expense. In the past, the linear and nonlinear characteristics during transient vehicle acceleration and deceleration of the dual-mode scramjet combustor have been obtained solely from flight test. The construction of a transient trajectory facility at CAS enables studies on the transient performances from ground experiments at low cost. Thus, the purpose of the paper is twofold: first, to evaluate the linear and nonlinear characteristics of a DMSJ combustor during the simulated acceleration and deceleration process, and second, to develop a modeling scheme based on historical measurements aiming for online prediction and control.

II. EXPERIMENTAL SETUP

A. Experimental facility

The experiments were carried out in the direct-connected transient flight trajectory simulator 1 (FTS-1) at the Institute of Mechanics, Chinese Academy of Sciences. The FTS-1 consists of a compressed gas supply system, a water-cooled hydrogen-burning vitiator, a water-cooled variable De Laval nozzle, a testing section, and an integrated control system. The facility is detailed in our previous study.[22] The hydrogen-burning vitiator supplements oxygen to ensure that the volume fraction of oxygen in the combustion gas is consistent with the atmosphere, and water vapor is introduced at the same time. The mass flow rate of the air, oxygen, and hydrogen and the De Laval nozzle flow path are coordinated to simulate the transient acceleration and deceleration processes. The measured vitiator total pressure during the two experiments is shown in Fig. 1, and the detailed experimental parameters are summarized in Table I.

The schematic diagram of Fig. 2 is an illustration of the test section, which includes an $80 \times 40\ \text{mm}^2$ constant area isolator, a single expansion model combustor with an inclination angle of 2°, and double cavity flameholders. The two cavities are of the same size, and the first cavity is located 447 mm downstream of the inlet of the isolator. The length, depth, and angle of the trailing edge of each cavity are 65, 17 mm, and 22.5°, respectively. The kerosene injection module with a row of six injection ports of 0.3 mm and the pilot hydrogen injection module are installed at 60.5 and 9.5 mm upstream of the cavity, respectively. The spark plug is marked as a red star in Fig. 2 and installed at the bottom of the first cavity. In addition, a pair of quartz glass windows is installed on both sides of the first cavity for the flow and combustion field visualization and illustrated as the red dashed box in Fig. 2. High-frequency sensors, Kulite XTL-190(M), with a sampling rate of 50 kHz were mounted in the cavity, and the central one located at 27.5 mm upstream of the cavity rear edge was used for latter analysis. The high-frequency sensor is simultaneously triggered with Phantom cameras through DG645 signal delay generator, and another synchronization DG645 is used as the external clock of the two imaging cameras. One high-speed camera Phantom V2612 for capturing the CH^* chemiluminescence is equipped with a bandpass filter. The filter has a center wavelength of 430 nm, a bandwidth of 10 nm, and a peak transmittance of 0.882. The camera exposure time is 20 μs at the frame rate of 6000 frames per second, and the resolution is 1280 pixels × 800 pixels. Flow field visualization is acquired by the traditional z-type schlieren system with a continuous light source, and the schlieren system camera has an exposure time of 2 μs, a frame rate of 6000 frames per second, and a resolution of 1920 pixels × 700 pixels.

III. RESULTS

A. Engine working mode

The evolution of the axial pressure distribution, which is plotted in the form of three-dimensional time-space diagrams, and the corresponding Mach number of the flight envelope ABC and CBA are shown in Fig. 3. The inlet of the isolator is used as the starting point of the flow direction discussed in the paper, as shown in Fig. 2, and the

TABLE I. Experimental parameters.

Trajectory	Simulated flight Mach number	Simulated flight altitude/km	Simulated dynamic pressure/kPa	Simulated total pressure/kPa	Simulated total temperature/K	Total flow of heating gas/($g \cdot s^{-1}$)	Kerosene flow/($g \cdot s^{-1}$)
ABC	5.0–5.6–6.0	20.99–23.93–26.28	82–64–50	1548–1678–1939	1249–1475–1648	1878–1283–1178	≈28
CBA	6.0–5.6–5.0	26.28–23.93–20.99	50–64–82	1939–1678–1548	1648–1475–1249	1178–1283–1878	≈28

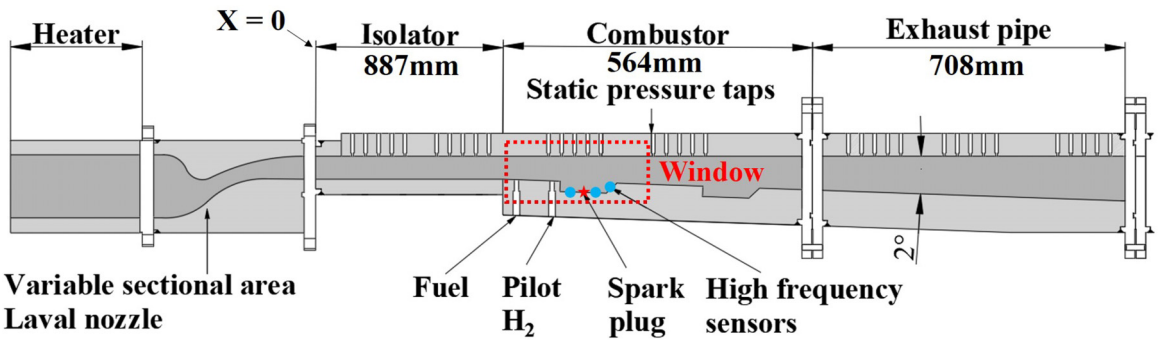

FIG. 2. Detailed schematic diagram of the test section.

pressure is dimensionless using the first pressure measuring at the inlet entrance. The method for calculating the Mach number can be found in our previous publication.[22] The black plane is a representation of where the Mach number equals unity. For the acceleration envelope ABC, it is obvious that there is a high pressure region in the isolator, accompanied by a subsonic Mach number, indicating the presence of the pseudo-combustion shock train systems. The pseudo-combustion shock train remains stabilized in the second cavity until the pilot hydrogen is cut off at 16.5 s from the experiment initialization as shown in Figs. 3(a) and 3(c), and the location of high pressure region and low Mach number area are well maintained. The model combustor operates in ramjet mode from 14.5 to 19.0 s, and as the flight trajectory accelerates, the back pressure of the pseudo-combustion shock train disappears and the Mach number of the entire flow path

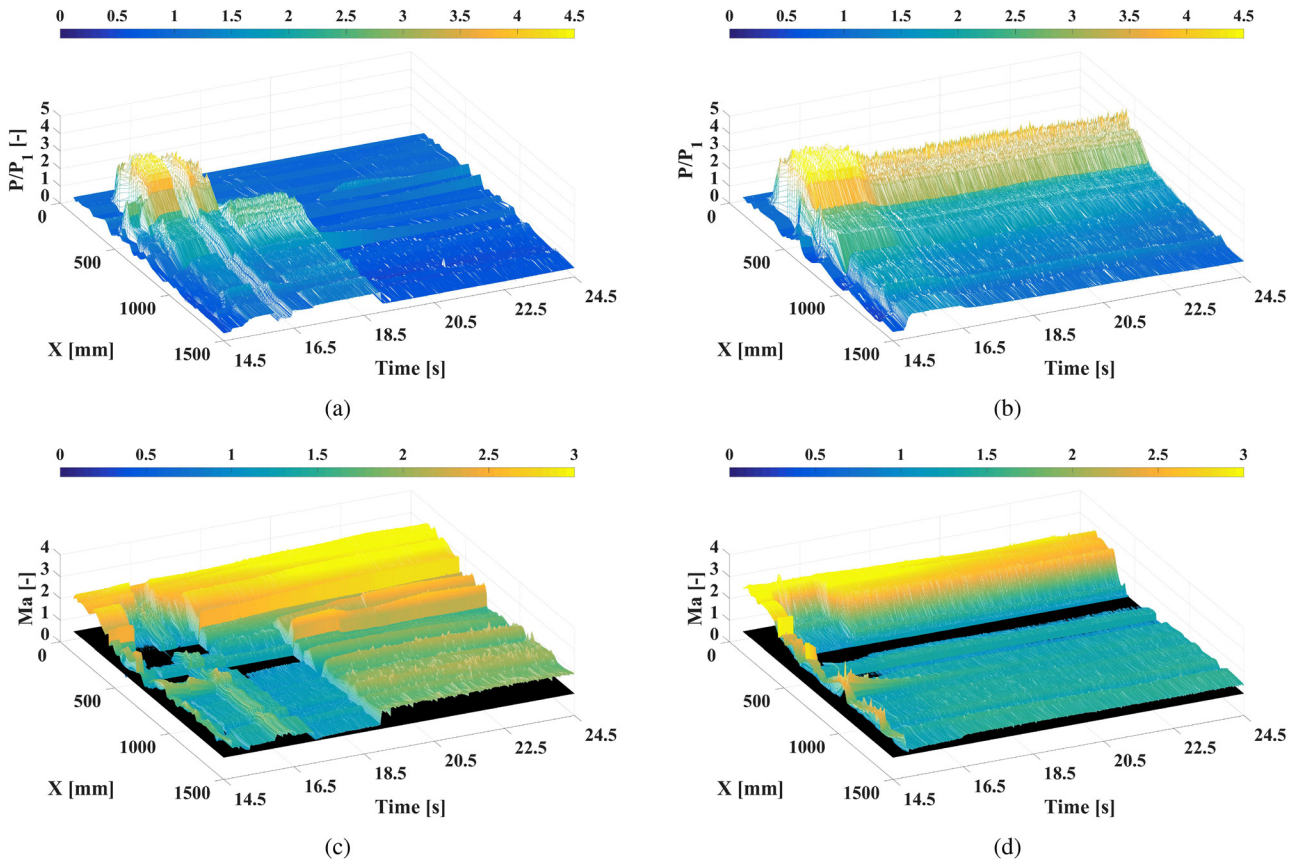

FIG. 3. Time history of the pressure distribution of (a) trajectories ABC and (c) CBA and Mach number distribution of (b) ABC and (d) CBA.

becomes supersonic as shown in Fig. 3(c). The combustor is considered to operate in the scramjet mode from 19.0 to 24.5 s. In contrast to the acceleration process, the combustor operates solely in the ramjet mode of the deceleration trajectory of CBA. The equivalence ratio decreases with the decrease in Mach number, while the high pressure region and the low Mach area in the isolator remain basically unchanged, which indicates that a transient balance has been established between the heat addition and the flow variation in the combustor. This finding is consistent with our previous study of the transient acceleration process.[22]

B. Linear analysis

The oscillation characteristics of the acceleration and the deceleration trajectory are evaluated by the linear decomposition analysis methods. Figure 4 shows time history of the high-frequency pressure and its corresponding spectrum diagram of trajectories ABC and CBA. In the case of ramjet mode, strong oscillation is observed, while in the case of scramjet operation, the oscillation becomes weaker suggesting a transition of the governing flow mechanism from the subsonic turbulent combustion in the cavity to supersonic combustion as the pseudo-combustion shock train dissipates. A broadband oscillation between 0 and 2 kHz exists in both ramjet and scramjet mode, which is governed by the flow oscillation of the cavity itself. In addition, the combustion-induced heat release in the case of ramjet mode seems to enhance the amplitude of the combustion oscillation, while the oscillation is barely affected by the heat addition in the case of scramjet operation. As the low-frequency oscillation is usually considered to be a critical characteristic that would induce potential structural damage and failure, attention is given here. The low-frequency oscillation was observed to mainly occur from 17 to 19 s of the trajectory ABC. Thus, to elucidate the governing mechanism responsible for the low-frequency combustion oscillation during acceleration, 18.0–18.5 s of trajectory ABC is analyzed in detail in the following section.

The basic flame and flow characteristics during the low-frequency oscillation in 18.0–18.5 s of trajectory ABC are quantified and evaluated. Figure 5 shows the temporal average, the standard deviation of CH^* images, and the instantaneous schlieren image in 18.0–18.5 s. The flame is mainly stabilized in the shear layer, with intermittent oscillations into the cavity. For the flow structures of low-frequency combustion oscillation, the main flow characteristics are the separation wave at the front edge of the cavity and the motion of the shear layer in the cavity, as shown in Fig. 5. Alternating oscillations between the cavity shear layer and the cavity recirculation zone are observed. In this paper, we define the reflection point x_{rfl} of the separation wave and the angle between the upper edge and the lower wall of the cavity shear layer α_c as the two quantities for the evaluation of

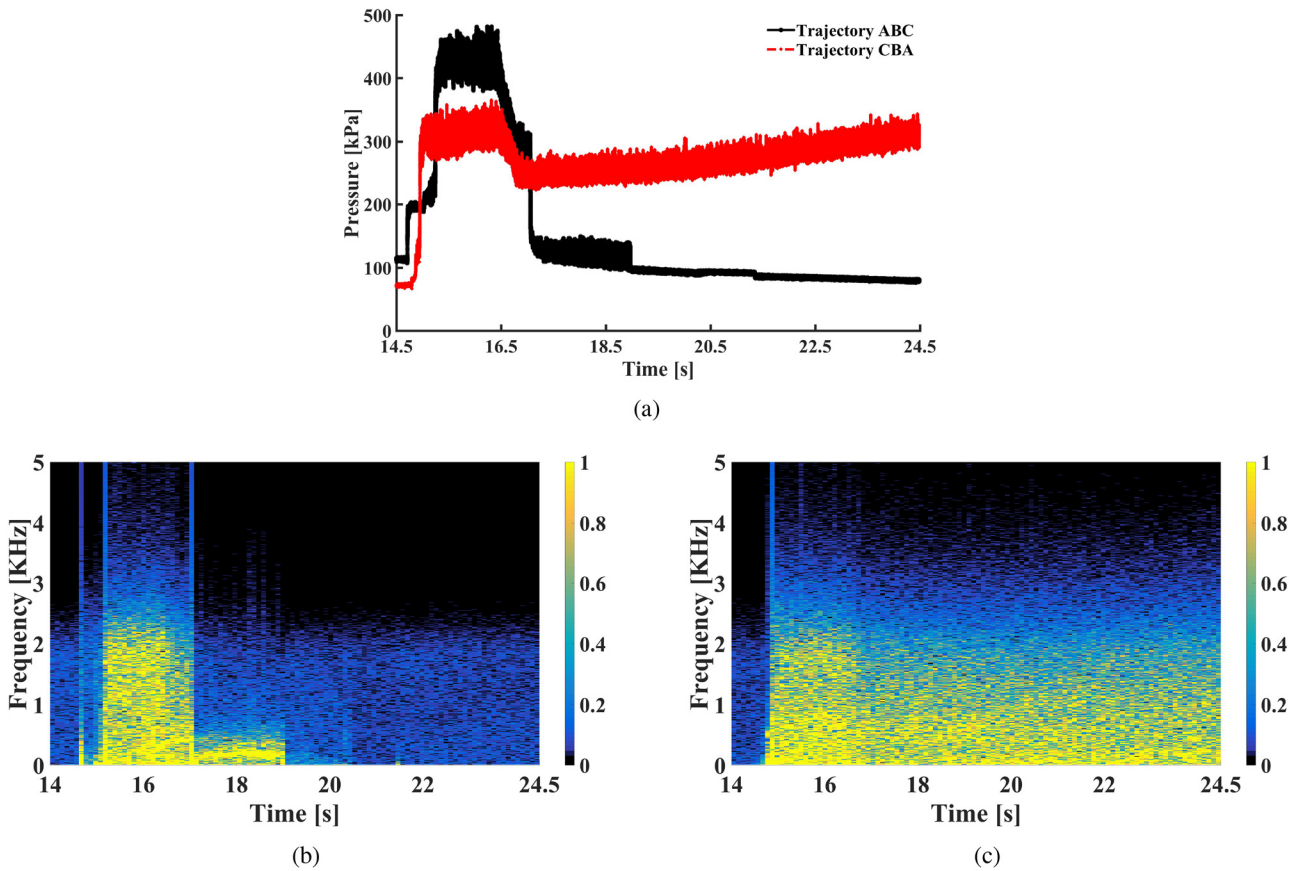

FIG. 4. (a) Time history of high-frequency pressure for trajectories ABC and CBA and their corresponding spectrum diagram: (b) ABC and (c) CBA.

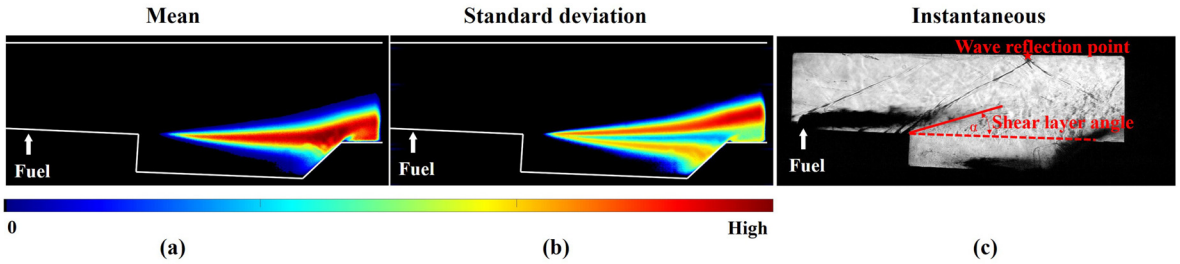

FIG. 5. Flame and flow oscillation characteristics of trajectory ABC 18.0–18.5s: (a) the temporal averaged CH* chemiluminescence, (b) the standard deviation of CH* chemiluminescence, and (c) an instantaneous schlieren image.

low-frequency combustion oscillation dynamics. These two parameters are considered to represent the physical process of the shock wave and the recirculation zone interactions. This assumption is studied in detail in the following section.

Figure 6 shows the time history of the angle between the cavity shear layer upper edge and the lower wall α_c. During acceleration, the angle α_c remains relatively stable and oscillates between $-5°$ and $5°$, suggesting intermittent flow movement of the shear layer into the cavity and lack of response to either the equivalence or the accelerated Mach number.

Figure 7 demonstrates the time history of the reflection point x_{rfl} of the separation wave. The separation wave at the cavity leading edge oscillates violently during acceleration. The reflection point x_{rfl} varies between 55 and 80 mm from the cavity leading edge as shown in Fig. 7(a). This is induced by the periodic back pressure movement caused from the heat addition. A partially enlarged plot is shown in Fig. 7(b). The periodic process is clearly observed, which includes the generation, the axial propagation, and the dissipation. In addition, the propagation velocity of the reflection point x_{rfl} is found to be in the range of 10.7–16.3 m/s. The difference in the propagation velocity is likely to be governed by the temporal difference in the heat release rate, as it is a direct indication of the periodic back pressure movement from the heat addition.

Based on the above quantitative analysis, the low-frequency oscillation process is considered to be closely related to the shock wave and the recirculation zone interactions, represented by x_{rfl} and α_c. As the reflective shock wave is governed by the flow structure of back pressure induced by the heat addition, Fig. 8 shows the time history of the integration of the CH* chemiluminescence images as a representation of the heat released I_{total}, defined as $I_{\text{total}} = \sum_{i=1}^{R}\sum_{j=1}^{C} I_{i,j}$, where $I_{i,j}$ represents the intensity value at row I and column J of CH* chemiluminescence, and R and C represent the total number of rows and columns, respectively. The instantaneous value of I_{total} of trajectory ABC at 16.5 s is used for dimensionless. Oscillations of the heat

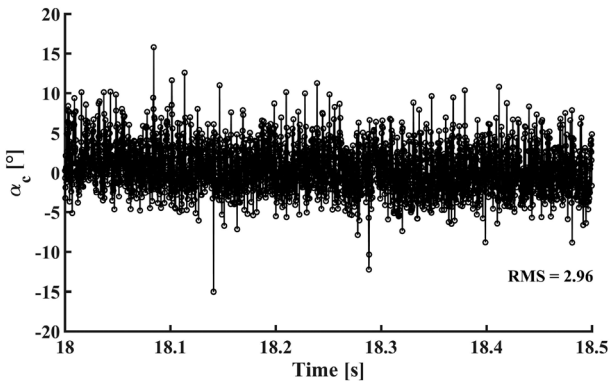

FIG. 6. Time history of the angle α_c between the cavity shear layer upper edge and the lower wall.

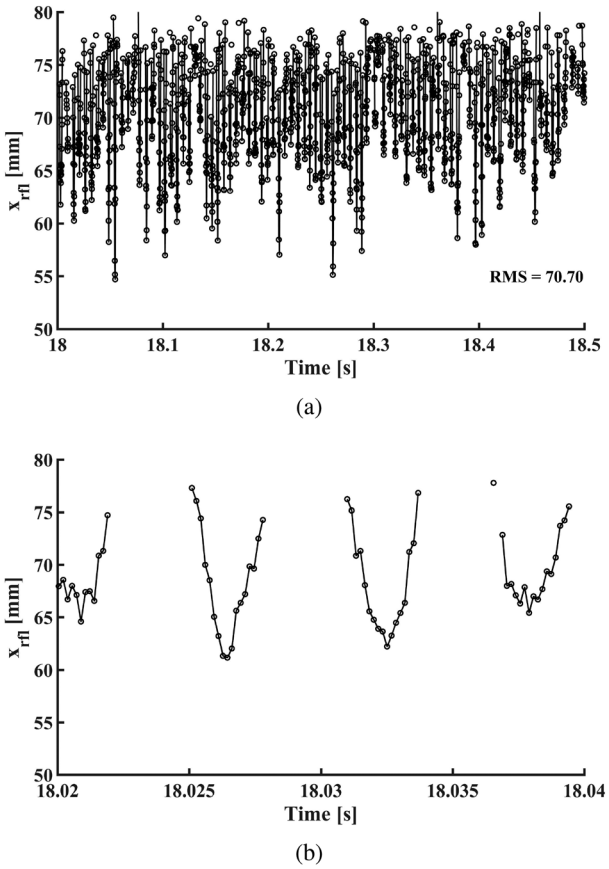

FIG. 7. Time history of (a) the reflection point of the separated wave at the leading edge of the cavity on the upper wall x_{rfl} and (b) the partial enlarged view.

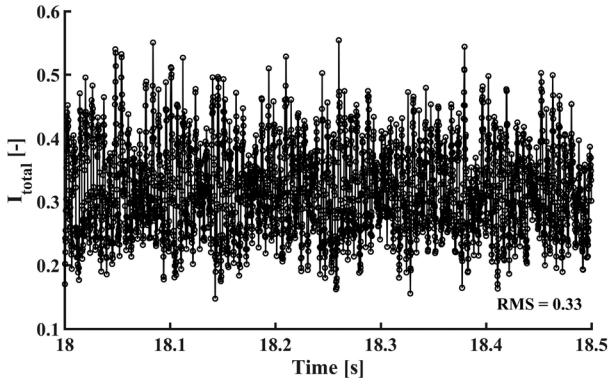

FIG. 8. Time history of I_{total}.

released I_{total} are observed and compared with that of x_{rfl} and α_c in the following sections.

Before moving forward to study the temporal cross-correlations between x_{rfl}, α_c, and I_{total} to elucidate the governing mechanism of the low-frequency combustion oscillation, the power spectra of the shear layer angle α_c is evaluated in Fig. 9. There are three sharp peaks in the FFT signal, demonstrating that this oscillation process is controlled by three dominant frequencies. In addition, the three dominant frequencies of the shear layer angle are consistent with that of the high-frequency pressure in the cavity, indicating that the two belong to the same physical process. Similar to the cavity shear layer angle α_c, the three main frequencies of the FFT of the separation wave location x_{rfl} and the heat released I_{total} are also consistent with the high-frequency pressure oscillation as shown in Fig. 9. Thus, efforts are given to cross-check that the three defined quantities represent the same flow dynamics.

To elucidate the governing mechanism of the low-frequency combustion oscillation process, a numerical method of dynamic mode decomposition (DMD) is adopted to evaluate the 3000 CH* chemiluminescence high-speed images. DMD is a popular and efficient method for structure extraction at a desired frequency.[23,24] In this paper, the criterion proposed by Kou and Wang.[25] was used to select dominant modes from DMD. The first four modes extracted by the DMD method are illustrated in Fig. 10. Mode 0 is equivalent to the

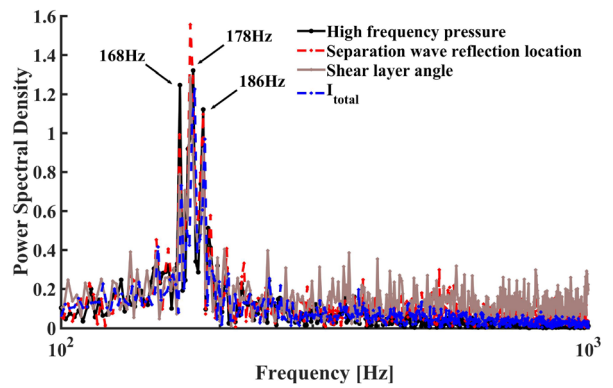

FIG. 9. Power spectra of flow and flame parameters.

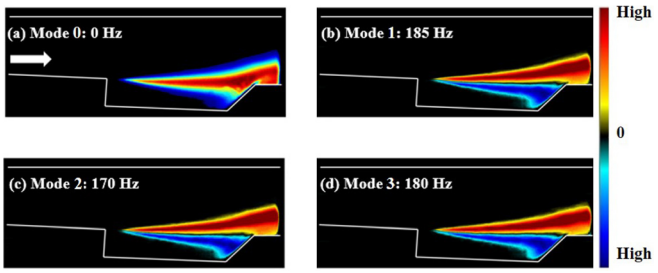

FIG. 10. The first four modes extracted through the DMD method.

temporal mean image in Fig. 5, and the modes from 1 to 3 capture the first three-order combustion oscillation process, and their three corresponding frequencies are 170, 180, and 185 Hz, which are consistent with the dominant frequencies of the cavity high pressure of 168, 178, and 186 Hz. This suggests that x_{rfl}, α_c, and I_{total} are indeed a good representation of the low-frequency combustion oscillation. Thus, the initial assumption of this section is approved with confidence that the low-frequency oscillation process is governed by the shock wave and the recirculation zone interactions.

The oscillation in one periodic cycle is shown in Fig. 11. The angle α_c filtered out oscillations above 300 Hz is shown here for better presentation. According to the characteristics of the flow and flame dynamics, the oscillation is categorized into four phrases and summarized as follows.

Phase 1: The shear layer moves toward the mainstream, causing the flame to transform into cavity shear layer flame combustion mode. The strong heat release induced by the cavity shear layer flame gradually forms back pressure. At this time, there is no shock train in the mainstream.

Phase 2: Under the action of the cavity recirculation zone, the shear layer continues to rise to the outside of the cavity. The fuel convects downstream along the shear layer to form shear layer flame, leads to the increased heat release and the formation of back pressure. The shock train propagates upstream under the strong heat release.

Phase 3: The large consumption of combustion products in the cavity weakens the effect of the shear layer and the recirculation zone. The shear layer begins to move into the cavity, and the combustion heat is gradually weakened, causing the shock train to move downstream.

Phase 4: The shear layer returns to the cavity, and the flame is transformed into cavity flame, accumulating heat for the next shear layer lift. At this time, the heat release is too low to form a back pressure, and the shock train in the mainstream is completely dissipated.

The oscillation in one periodic cycle clearly shows the physical mechanism of low-frequency oscillation, and attempts are given for short-term flame prediction based on the physical process. Figure 12 shows the time coefficients of the first three DMD modes. For each mode, the initial amplitude and the growth rate can be obtained by

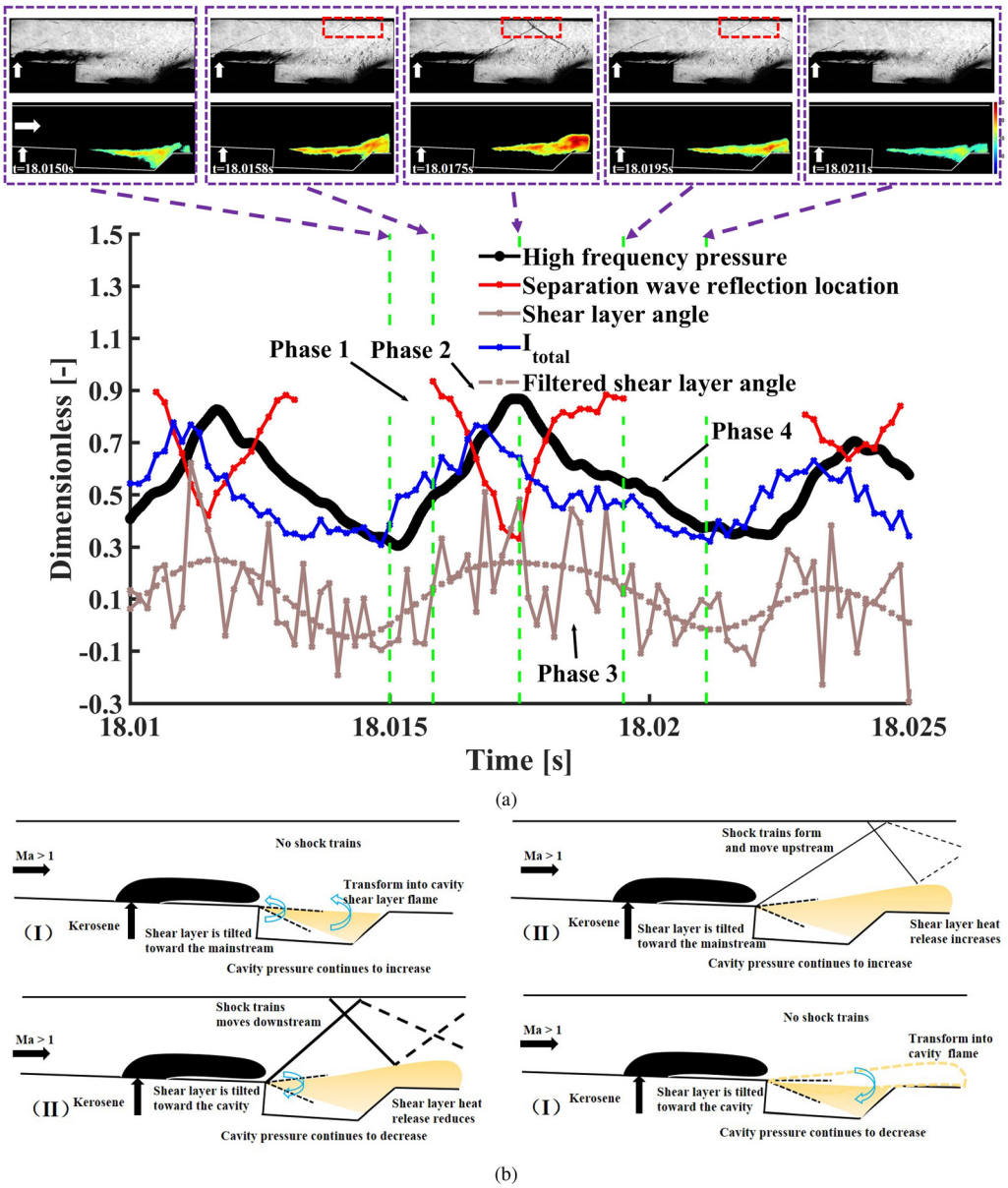

FIG. 11. Oscillation mechanism (a) in one cycle and (b) corresponding schematic diagram.

DMD. A reasonable assumption is that all modes still have the same growth rate for a short period of time in the future, such that the prediction can be made based on this assumption.

To test the prediction accuracy of DMD, the DMD modes of 1500 CH^* images from 18.0 to 18.25 s were analyzed together with the corresponding time coefficients to make prediction. The correlation coefficient between predicted and experimental I_{total} is used to evaluate prediction accuracy, as shown in Figs. 13 and 14. A qualitative and quantitative comparison between prediction and experiment measurements from 18.25 to 18.5 s suggests the consistency and high accuracy of short-term prediction.

C. Nonlinear analysis

In the section of linear analysis, the combustion oscillation characteristics of the acceleration and deceleration trajectories ABC and CBA are shown in Fig. 4. Fichera *et al.*[26] pointed out that the broadband oscillation usually indicates that the linearity assumption of the FFT does not hold and implies the underlying nonlinearity of the dynamic system, which in our case is physically resulting from the interactions between the fluid dynamics and chemical reaction. Therefore, it is necessary to understand the nonlinear dynamic behavior of the system. In this section, the nonlinear time series (NLTS) analysis is applied to quantify the nonlinear characteristics of the dynamic system.

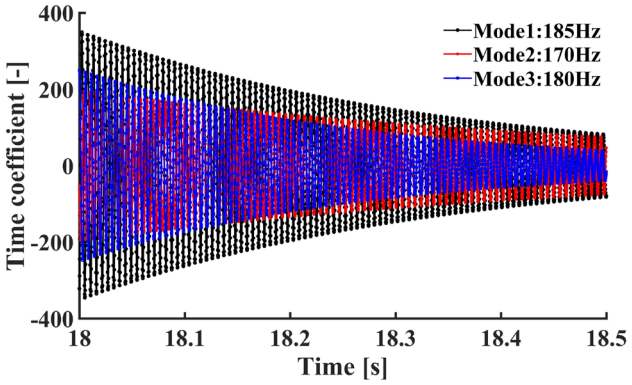

FIG. 12. Time coefficient of the first three modes extracted through the DMD method.

A special feature of the NLTS is the introduction of the concept of phase space and the method of delays. The reconstructed phase space and the original time series share the same features in many ways,[27] thereby having been widely applied to quantify the nonlinear characteristics of the system. The most common way to reconstruct a phase space is by performing the uniform time interval measurements referred to as uniform time delay reconstruction (UTD). The procedure of the UTD is briefly explained herein. The reconstructed phase space vector $\vec{R}$ is as follows:

$$\vec{R} = [y(t), y(t+\tau), \ldots, y(t+(m-1)\tau)] = \begin{pmatrix} y(t_1) & y(t_1+\tau) & \cdots & y(t_1+(m-1)\tau) \\ y(t_2) & y(t_2+\tau) & \cdots & y(t_2+(m-1)\tau) \\ \vdots & \vdots & \ddots & \vdots \\ y(t_n) & y(t_n+\tau) & \cdots & y(t_n+(m-1)\tau) \end{pmatrix}, \quad (1)$$

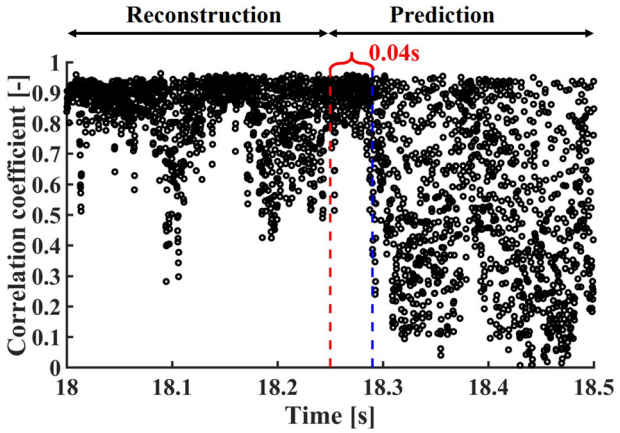

FIG. 14. Correlation coefficient between experimental and predicted I_{total} as a function of time.

where $y(t)$ is the first n point of the observed time series, m and τ are the embedding dimension and time delay, respectively. The row of the reconstructed phase space n can be obtained by

$$n = N - (m-1)\tau, \quad (2)$$

where N is the total length of the observed time series.

The embedding theorem ensures the geometric object defined by the vectors $y(t)$ is "equivalent" to the original trajectory.[28] In 1981, Takens[29] proved the existence of diffeomorphism between the original and the reconstructed attractors for the noise-free measurements with unlimited length, an arbitrarily chosen time delay τ, and a sufficiently large embedding dimension m. However, measurements in reality are often accompanied by noise and with finite length; thus, the improper selection of embedding parameters would significantly distort the reconstruction according to this methodology. Therefore, the

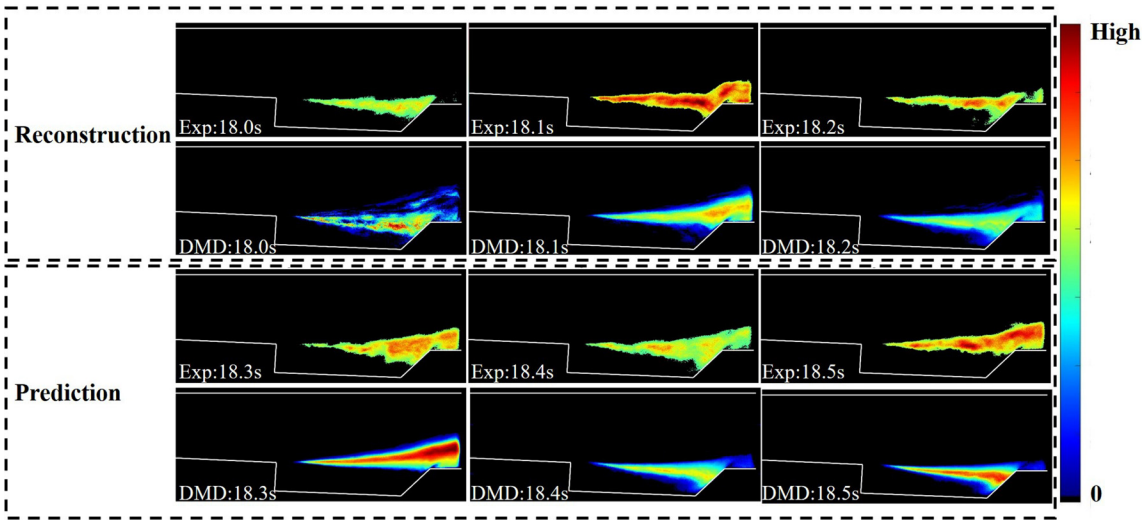

FIG. 13. Comparison of the DMD reconstruction and prediction.

definition and selection of embedding parameters is critical in the nonlinear time series analysis.

Evaluations of the embedding parameters are described in the following sections based on the axial pressure measurements of the acceleration and deceleration trajectories ABC and CBA. In this section, the high-frequency pressures from 16.0 to 16.5 s of trajectories ABC and CBA were examined as an example of the reconstruction process. The time delay τ should be neither too large nor small. If the time delay τ is too small, the reconstructed phase space would be highly folded and results in distortions, and if the time delay τ is too large, the reconstruction would appear to follow random distribution. The mutual information (MI) $I(X, Y)$ approaches zero if only the two random variables are strictly independent.[30,31] Thus, in this paper, the mutual information $I(X, Y)$ and the correlation dimension D_2 were calculated for the appropriate selection of the time delay τ and the embedding dimension m, respectively.[28] The mutual information $I(X, Y)$ between the two random variables X and Y is defined as

$$I(X, Y) = \sum_i \sum_j p(x_i, y_j) \log_2 \frac{p(x_i, y_j)}{p(x_i)p(y_j)}, \tag{3}$$

where $p(x_i, y_j)$ is the joint probability distribution function of X and Y, and $p(x_i)$ and $p(y_j)$ are the marginal probability distribution functions of X and Y, respectively. $y(t)$ and $y(t + \tau)$ are defined as X and Y for the calculation of the mutual information. The first local minimum is defined as the chosen time delay τ in this paper. Figure 15 shows the process of the selection of τ based on the mutual information assumption, and $\tau = 12$ and $\tau = 15$ are, respectively, considered as the time delays for the phase space reconstruction of trajectories ABC and CBA.

The reconstruction dimension of the phase space defines its corresponding attractor. The minimum embedding dimension can be determined from the measurement of the geometric fractal dimension of the attractor,[28] which is defined by the correlation dimension D_2 derived by the Grassberger–Procaccia algorithm.[32] The derivation of Grassberger–Procaccia algorithm is briefly described as follows.

The distances between every two adjacent rows r_i and r_j of the reconstructed phase space $\vec{R}$ is first calculated as follows:

$$d_{ij} = \| r_i - r_j \|_F, \tag{4}$$

where $\| \cdot \|$ represents the Frobenius norm.

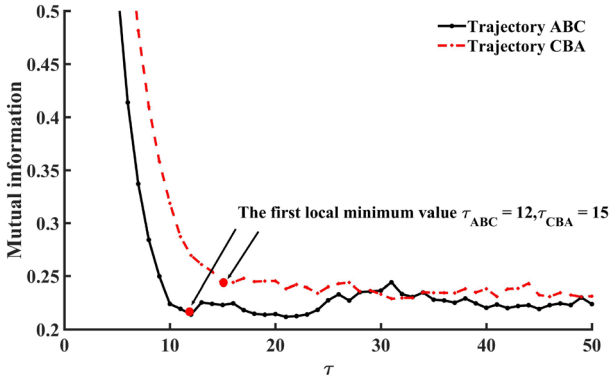

FIG. 15. Mutual information defined as a function of time delay τ.

The correlation integral function $C(r)$ is then defined as

$$C(r) = \frac{2}{n(n-1)} \sum_{i=1}^{n} \sum_{j=1}^{n} H(r - d_{ij}), \tag{5}$$

where H is the Heaviside function,

$$H(r - d_{ij}) = \begin{cases} 1, & r >= d_{ij}, \\ 0, & r < d_{ij}. \end{cases} \tag{6}$$

The estimated correlation dimension of an attractor, D_2, is the exponent in a power law scaling the correlation integral to distance when r is small,

$$C(r) \propto r^{D_2}, \tag{7}$$

such that D_2 is calculated based on the slope of the curve $\ln C(r)$–$\ln r$, and the embedding dimension can be determined as the closest integer larger than D_2. The curve of $\ln C(r)$–$\ln r$ and the slope defining D_2 are shown in Fig. 16. As described above, the primary slope of the curve in the smaller region of r represents D_2. For each of the embedding dimension m, a corresponding D_2 is calculated, as shown in Fig. 16. With the increase in the embedding dimension m, D_2 gradually increases and reaches a plateau, which means that D_2 has basically reached the fractal dimension of the attractor, and the value of embedding dimension m is determined as the integer above the plateau.[28] In Fig. 16, D_2 is finally stabilized at around 9.8 for trajectory ABC, and the nearest integer above 9.8 is 10. Therefore, the appropriate value of the embedding dimension m is chosen as 10. In a similar way, m is chosen as 9 for trajectory CBA. It should be pointed out that the selection of the number of fitting points has an impact on the final value of m, so the two-dimensional projection of the attractor is given later.

The phase space $\vec{R}$ can be reconstructed by Eq. (1) with the embedding parameters m and τ pre-determined. The dynamic evolution of the two-dimensional attractor based on the high-frequency pressure of the trajectories ABC and CBA are shown in Fig. 17. $P(t)$ indicates the observed high-frequency pressure time series, and the $P(t + \tau)$ represents the corresponding delays. The high-frequency pressure for each time period is normalized by its maximum value for this comparison. It should be pointed out that the attractor from 17.5 to 18.5 s of the trajectory ABC is missing due to the presence of strong linearity, which results in a void of a local minimum of the mutual information evaluation. The morphology of the attractor is similar to that obtained from other studies on flame dynamics.[26,33,34] This kind of attractor has a complex structure in the middle, and the two ends are similar to the ring structure. Fichera *et al.*[26] pointed out that the complex systems from experimental observations may be further investigated by comparing them with a known mathematical system of similar morphological characteristics. The attractor basically maintains similar morphological characteristics for both the ramjet mode and the scramjet mode. This is a strong implication that there are similarities in the nonlinear systems of the two working modes, and the acceleration or deceleration process has little influence on the nonlinear dynamic systems.

The above analysis is the qualitative nonlinear characteristics of the system, and the quantitative nonlinearity of the acceleration process and deceleration process is given by Shannon entropy of the high-frequency pressure. Since the Shannon entropy is a classic method from the 1940s, detailed definitions are neglected and only a few lines

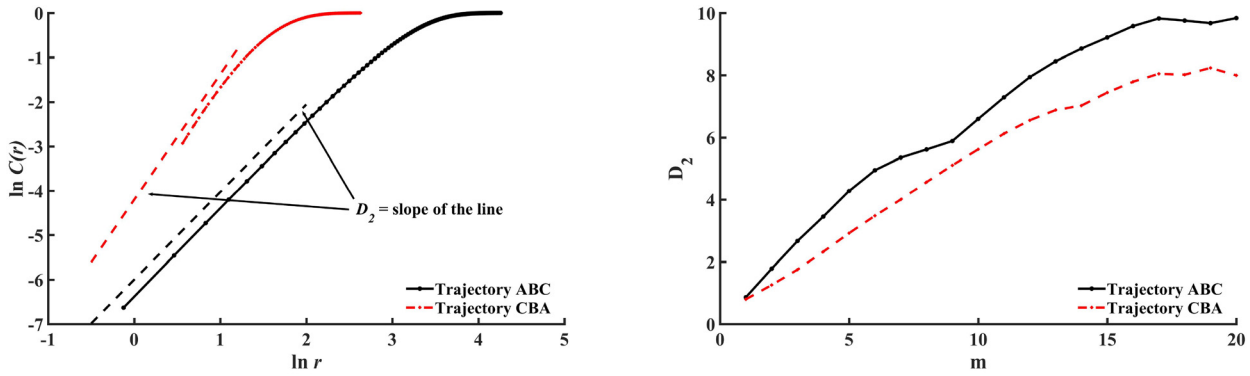

FIG. 16. Parameter selection of reconstructed time-delay matrix: (a) D_2 and (b) the embedding dimension m.

of descriptions are given. A dynamic system is highly uncertain and likely random when the Shannon entropy approaches unity and nonlinear modeling is a necessity. On the contrary, the dynamic system is certain and deterministic when the Shannon entropy deviates from unity, and in this case, the linear modeling method applied. The Shannon entropy of the high-frequency pressure is evaluated based on the definition of

$$H_s = -\frac{1}{\log n_{\text{seq}}} \sum_k p_k \log p_k, \tag{8}$$

where p_k is the probability of the occurrence of sequence, and n_{seq} is the number of different sequences of the time series k.

Figure 18(a) illustrates a parameter sweep in determining the Shannon entropy sequence length L and the partition N with applications on the high-frequency pressure measurements of the trajectories ABC and CBA. Three characteristic phases of trajectory ABC are evaluated including the ramjet mode phase (16.0–16.5 s), the phase of the low-frequency combustion oscillation (18.0–18.5 s), and the phase of the scramjet mode (22.0–22.5 s). The combination of the sequence length L and the partition N is selected when it yields the minimum saddle point of the Shannon entropy.[35] Based on the parameter sweep, 4 and 2 are, respectively, adopted as the sequence length L and the partition N for both the acceleration trajectory ABC and deceleration CBA Shannon entropy evaluations.

Figures 18(b) and 18(c) show that the Shannon entropy is in general below 0.7 for both the acceleration and the deceleration trajectories, so that the system is deterministic with certain degree of certainty, which suggests the presence of governing physical mechanisms. This gives confidence of the possibility to develop a physics-based predictive model of the dual-mode scramjet combustor for both the acceleration and the deceleration trajectories. For the acceleration trajectory ABC, the Shannon entropy varies between 0.3 and 0.7, and a transition with a decreased level of the Shannon entropy is observed from 17 to 19 s. The decreased level of the Shannon entropy suggests the strong presence of the underlying physical process. Since this specific transition period coincides with the phase of low-frequency combustion oscillation analyzed in detail above, it is very likely that the pseudo-combustion shock train system and oscillations between the shear layer and the cavity contribute to the decreased level of Shannon entropy. The Shannon entropy of the deceleration trajectory maintains around 0.57 all the time, indicating that the pseudo-combustion shock

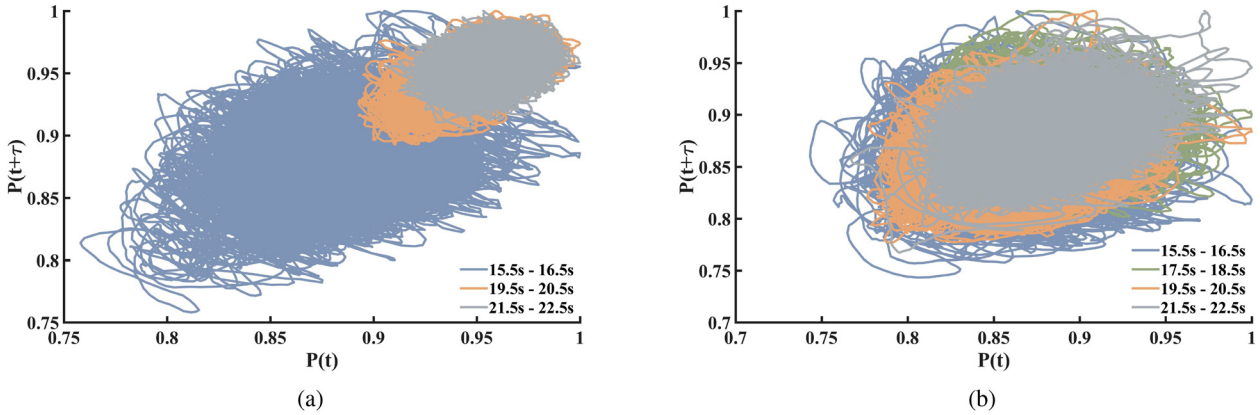

FIG. 17. Dynamic evolution of two-dimensional attractor based on high-frequency pressure for (a) trajectories ABC and (b) CBA.

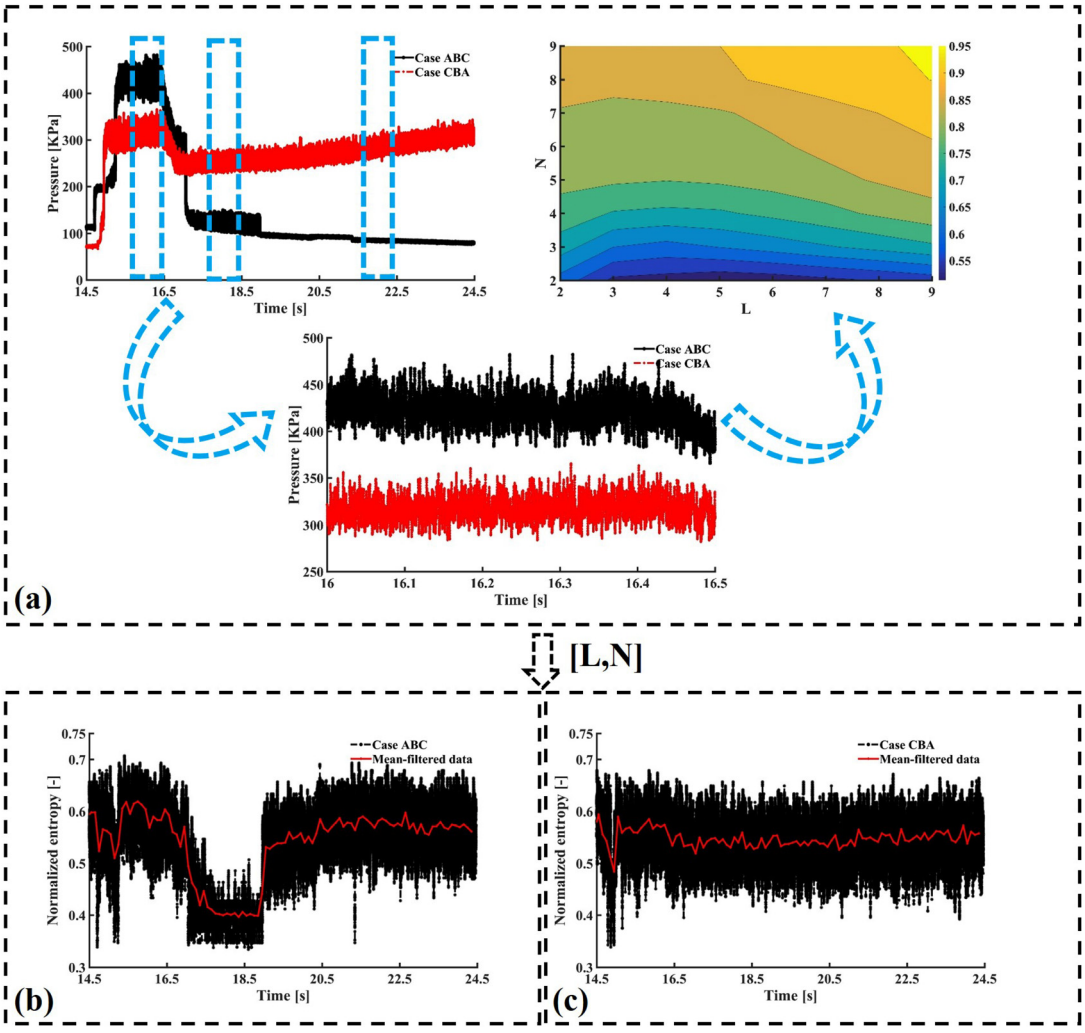

FIG. 18. Shannon entropy: (a) parameter sweep of the sequence length L and the partition N, (b) trajectories ABC, and (c) CBA.

train system is stable for the ramjet mode operation detailed in Sec. III A. The quantitative analysis result of Shannon entropy is consistent with that of the attractor, which further proves the similarity of the nonlinear characteristics of the ramjet mode and scramjet mode.

D. Predictive model

Based on the above analysis, the physical processes of acceleration and deceleration in general represent similar nonlinear characteristics. The linear characteristics are limited to the low-frequency oscillation period. Thus, a predictive model based on the nonlinear characteristics is proposed due to its generality for the acceleration and deceleration trajectory-oriented dual-mode scramjet combustor. The modeling method based on NLTS is that its core idea is to find the k nearest points of the ith point in the state space, and weight the nearest points as the prediction point $X(t)$.[36–38] For the nearest neighbors $X(i)$, $i \in K$, the exponential weight υ_i is given based on the Euclidean distances of $X(t)$,

$$\upsilon_i = e^{-\frac{\|X(t)-X(i)\|}{\min_{j\in K}\|X(t)-X(j)\|}}, \tag{9}$$

and the prediction can be obtained by

$$\hat{X}(t+1) = \frac{\sum_{i\in K} \upsilon_i X(i+1)}{\sum_{i\in K} \upsilon_i}. \tag{10}$$

To verify whether NLTS prediction is applicable to DMSJ, 5500 points of the high-frequency pressure time series measurement at 16.5 s in trajectory ABC were divided into two groups. The first 4500 points were used to construct the phase space and yielded the prediction of 1000 points, which are compared with the actual experimental measurements. The correlation coefficient is chosen as the evaluation criterion[39,40] to verify the prediction accuracy.

As the selection of the embedding dimension m and time delay τ is crucial for the nonlinear prediction.[41] The prediction error is

TABLE II. Correlation coefficients under different combinations of embedding parameters m and τ.

Embedding dimension m/delay time τ	3	4	5	6	7	8
5	−0.178	−0.253	0.226	0.943	0.669	0.669
6	0.248	0.226	0.853	0.464	0.669	−0.103
7	0.226	0.943	0.943	0.007	−0.050	−0.103
8	0.943	0.943	0.923	−0.050	−0.050	0.007
9	0.853	0.943	−0.103	−0.050	0.007	0.007
10	0.943	0.690	−0.050	−0.050	0.065	0.121
11	0.943	−0.050	−0.050	0.065	0.121	0.121

minimized following the method of Krakovská *et al.*[37,42] The correlation coefficient of 50 predicted points and its embedding dimension m and time delay τ are shown in Table II. The optimal combination is $(m-1)\tau = 27$–32.

The prediction with suitable embedding dimension m and time delay τ determined by the maximum correlation coefficient is shown in Fig. 19. It can be seen that the correlation coefficient is above 0.94 within 50 points, and it still remains around 0.65 at 100 points. This means that under the sampling frequency of high-frequency pressure of 50 kHz, the nonlinear model with suitable embedding parameters can accurately predict the pressure within 1–2 ms based on the historical measurement and proves the short-term high-precision prediction ability of the nonlinear model in DMSJ. As the number of prediction points increases, correlation coefficient decreases dramatically, indicating the long-term unpredictability of the system, which is typical in nonlinear system predictive models.

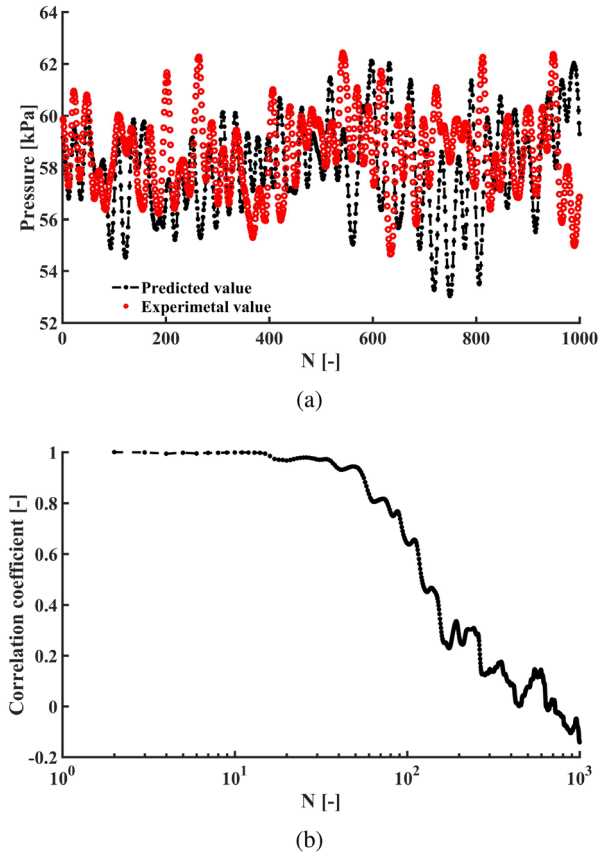

FIG. 19. (a) Comparison of experimental pressure and predicted pressure and (b) their correlation coefficient.

The predictive model of an acceleration trajectory-oriented dual-mode scramjet combustor is developed based on this method. First, 4950 plus 50 measurement points are selected for the phase space reconstruction and prediction, which corresponds to 0.1 s. The combination of the embedding dimension m and time delay τ are calculated based on the 4950 points. The 50 points predicted by the nonlinear model are compared with the measured points, and the combination of m and τ was chosen based on the maximum correlation coefficient. The interrogation window shifts 50 points and repeats the above process for model prediction. Figure 20 shows the predicted values per 1 ms, the true values, and their corresponding correlation of trajectories ABC and CBA. The predicted values are highly consistent with the experimental value, and the correlation coefficient between them is basically kept at 0.93, indicating the applicability of NLTS prediction in DMSJ acceleration and deceleration process. In addition, there is a relatively large error caused by the system linearity in the 17–19 s of the acceleration process ABC, which also corresponds to low Shannon entropy. It should be pointed out that the appropriate selection of m and τ here is obtained by comparing the predicted value and the actual value of different embedding parameter combinations. Robust solutions for optimizing the selection of embedding parameters should be further investigated to enable the application of the predictive model for online control purposes.

IV. CONCLUSION

In order to have the ability of trajectory-oriented online prediction and control of the dual-mode scramjet combustors, the linear and nonlinear characteristics of transient acceleration experiments are investigated. Based on the quantitative analysis, a predictive nonlinear modeling method of the acceleration trajectory-oriented dual-mode scramjet combustor is proposed and evaluated. The proposed model is capable of predicting the combustor performance with an acceptable accuracy of more than 1 ms, and the modeling methodology can be applied into other combustor. The main findings are summarized as follows:

- Three dominant frequencies of the combustion oscillations were observed in the acceleration trajectory based on the linear Fourier decomposition. For the low-frequency oscillation, which could be responsible for the structure damages, the DMD is applied on the corresponding CH^* chemiluminescence images. The periodic formation of the back pressure from the heat release and the interaction between the shear layer and the cavity is the governing mechanism contributing to the strong linearity.
- The nonlinear dynamic characteristics of the attractor and Shannon entropy were investigated. Similarities of the nonlinear characteristics between the ramjet mode and scramjet mode of the acceleration trajectory were observed based on the result of Shannon entropy, which is consistent with the attractor evaluations.

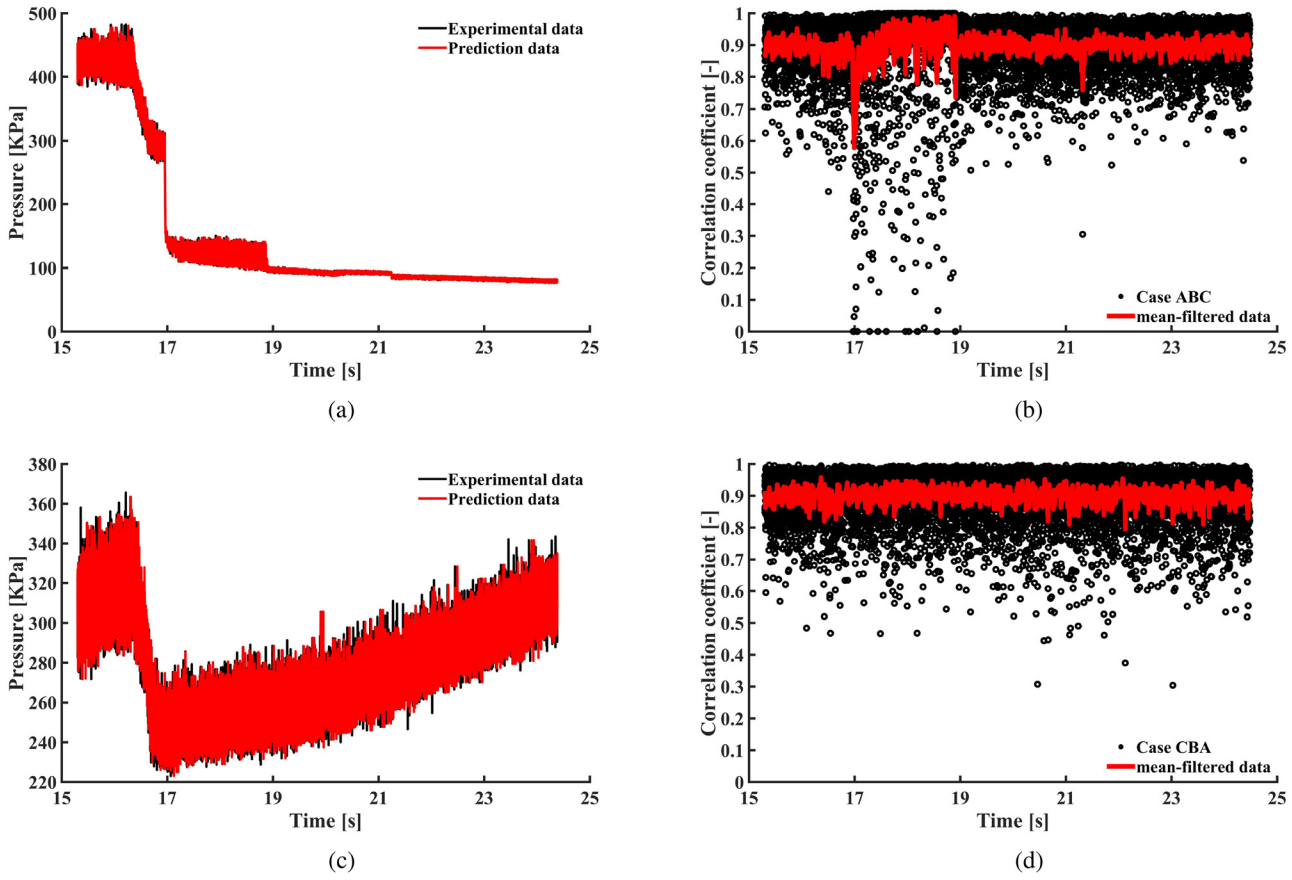

FIG. 20. High-frequency pressure prediction of 1 ms for (a) trajectories ABC and (c) CBA and their corresponding correlation efficient: (b) ABC and (d) CBA.

- A predictive modeling method based on the nonlinear characteristics is proposed due to its generality for the acceleration and deceleration trajectory-oriented dual-mode scramjet combustor. The proposed model is capable of predicting the combustor performance with an acceptable accuracy of more than 1 ms. Robust solutions for optimizing the selection of embedding parameters should be further investigated to enable the application of the predictive model for online control purposes.

ACKNOWLEDGMENTS

The authors acknowledge the financial support from the National Natural Science Foundation of China (Grant Nos. 91941104 and 11872366).

AUTHOR DECLARATIONS

Conflict of Interest

The authors have no conflicts to disclose.

Author Contributions

Ruixu Zhou: Conceptualization (equal); Data curation (equal); Formal analysis (equal); Funding acquisition (equal); Investigation (equal); Methodology (equal); Project administration (equal); Resources (equal); Software (equal); Supervision (equal); Validation (equal); Visualization (equal); Writing – original draft (equal); Writing – review & editing (equal). **Tuo Li:** Investigation (equal); Resources (equal); Software (equal); Validation (equal). **Xinyang Li:** Investigation (equal); Software (equal). **Huan Lian:** Conceptualization (lead); Data curation (supporting); Formal analysis (lead); Funding acquisition (lead); Investigation (supporting); Methodology (lead); Project administration (lead); Resources (lead); Software (equal); Supervision (equal); Validation (equal); Visualization (equal); Writing – original draft (equal); Writing – review & editing (equal).

DATA AVAILABILITY

The data that support the findings of this study are available from the corresponding author upon reasonable request.

REFERENCES

[1]E. T. Curran, "Scramjet engines: The first forty years," J. Propul. Power **17**(6), 1138–1148 (2001).
[2]Y. Tian, W. Shi, F. Zhong, and J. L. Le, "Pilot hydrogen enhanced combustion in an ethylene-fueled scramjet combustor at Mach 4," Phys. Fluids **33**(1), 015105 (2021).
[3]S. Priebe, J. H. Tu, C. W. Rowley, and M. P. Martín, "Low-frequency dynamics in a shock-induced separated flow," J. Fluid Mech. **807**, 441–477 (2016).

[4]J. H. Tu, C. W. Rowley, D. M. Luchtenburg, S. L. Brunton, and J. N. Kutz, "On dynamic mode decomposition: Theory and applications," J. Comput. Dyn. **1**(2), 391–421 (2014).
[5]P. J. Schmid, "Dynamic mode decomposition of numerical and experimental data," J. Fluid Mech. **656**, 5–28 (2010).
[6]P. J. Schmid, "Application of the dynamic mode decomposition to experimental data," Exp. Fluids **50**(4), 1123–1130 (2011).
[7]Y. Yuan, K. Zhou, W. Zhou, X. Wen, and Y. Liu, "Flow prediction using dynamic mode decomposition with time-delay embedding based on local measurement," Phys. Fluids **33**(9), 095109 (2021).
[8]J. Garicano-Mena, B. Li, E. Ferrer, and E. Valero, "A composite dynamic mode decomposition analysis of turbulent channel flows," Phys. Fluids **31**(11), 115102 (2019).
[9]F. Hamid, C. Sasmal, and R. P. Chhabra, "Dynamic mode decomposition analysis and fluid-mechanical aspects of viscoelastic fluid flows past a cylinder in laminar vortex shedding regime," Phys. Fluids **34**(10), 103114 (2022).
[10]H. Gotoda, H. Nikimoto, T. Miyano, and S. Tachibana, "Dynamic properties of combustion instability in a lean premixed gas-turbine combustor," Chaos **21**(1), 013124 (2011).
[11]H. Gotoda, K. Michigami, K. Ikeda, and T. Miyano, "Chaotic oscillation in diffusion flame induced by radiative heat loss," Combust. Theory Modell. **14**(4), 479–493 (2010).
[12]E. N. Lorenz, "Atmospheric predictability as revealed by naturally occurring analogues," J. Atmos. Sci. **26**(4), 636–646 (1969).
[13]S. Domen, H. Gotoda, T. Kuriyama, Y. Okuno, and S. Tachibana, "Detection and prevention of blowout in a lean premixed gas-turbine model combustor using the concept of dynamical system theory," Proc. Combust. Inst. **35**(3), 3245–3253 (2015).
[14]H. Gotoda, Y. Shinoda, M. Kobayashi, Y. Okuno, and S. Tachibana, "Detection and control of combustion instability based on the concept of dynamical system theory," Phys. Rev. E **89**(2), 022910 (2014).
[15]H. Chen, M. Guo, Y. Tian, J. Le, H. Zhang, and F. Zhong, "Intelligent reconstruction of the flow field in a supersonic combustor based on deep learning," Phys. Fluids **34**(3), 035128 (2022).
[16]Y. Li, J. Chang, Z. Wang, and C. Kong, "An efficient deep learning framework to reconstruct the flow field sequences of the supersonic cascade channel," Phys. Fluids **33**(5), 056106 (2021).
[17]C. Kong, J. Chang, Y. Li, and R. Chen, "Deep learning methods for super-resolution reconstruction of temperature fields in a supersonic combustor," AIP Adv. **10**(11), 115021 (2020).
[18]R. Gaudron and A. S. Morgans, "Thermoacoustic stability prediction using classification algorithms," Data-Centric Eng. **3**, e17 (2022).
[19]X. Deng, M. Guo, H. Chen, Y. Tian, J. Le, and H. Zhang, "Dual-path flow field reconstruction for a scramjet combustor based on deep learning," Phys. Fluids **34**(9), 095118 (2022).
[20]C. Kong, J. Chang, Y. Li, and Z. Wang, "A deep learning approach for the velocity field prediction in a scramjet isolator," Phys. Fluids **33**(2), 026103 (2021).
[21]C. Kong, Z. Wang, J. Zhang, X. Wang, K. Wang, Y. Li, and J. Chang, "Research on flame prediction in a scramjet combustor using a data-driven model," Phys. Fluids **34**(6), 066101 (2022).
[22]R. X. Zhou, F. Z. Meng, T. Li, Z. P. Li, and H. Lian, "Ram to scram mode transition in a simulated flight acceleration," Phys. Fluids **34**(6), 066114 (2022).
[23]P. W. Agostinelli, D. Laera, I. Chterev, I. Boxx, L. Gicquel, and T. Poinsot, "On the impact of H_2-enrichment on flame structure and combustion dynamics of a lean partially-premixed turbulent swirling flame," Combust. Flame **241**, 112120 (2022).
[24]J. Peng, Z. Cao, X. Yu, S. Yang, Y. Yu, H. Ren, Y. Ma, S. Zhang, S. Chen, and Y. Zhao, "Analysis of combustion instability of hydrogen fueled scramjet combustor on high-speed OH-PLIF measurements and dynamic mode decomposition," Int. J. Hydrogen Energy **45**(23), 13108–13118 (2020).
[25]J. Kou and W. Zhang, "An improved criterion to select dominant modes from dynamic mode decomposition," Eur. J. Mech.-B/Fluids **62**, 109–129 (2017).
[26]A. Fichera, C. Losenno, and A. Pagano, "Experimental analysis of thermo-acoustic combustion instability," Appl. Energy **70**(2), 179–191 (2001).
[27]N. H. Packard, J. P. Crutchfield, J. D. Farmer, and R. S. Shaw, "Geometry from a time series," Phys. Rev. Lett. **45**(9), 712–716 (1980).
[28]R. Huffaker, M. Bittelli, and R. Rosa, *Nonlinear Time Series Analysis with R* (Oxford University Press, 2017).
[29]F. Takens, "Detecting strange attractors in turbulence," in *Dynamical systems and Turbulence* (Springer, 1981), Vol. 366–381.
[30]A. Kraskov, H. Stogbauer, and P. Grassberger, "Estimating mutual information," *Phys. Rev. E* **69**(6), 066138, 2004.
[31]A. M. Fraser and H. L. Swinney, "Independent coordinates for strange attractors from mutual information," Phys. Rev. A **33**(2), 1134–1140 (1986).
[32]P. Grassberger and I. Procaccia, "Characterization of strange attractors," Phys. Rev. Lett. **50**(5), 346–349 (1983).
[33]T. Wang, Z. Wang, Z. Cai, M. Sun, H. Wang, Y. Sun, Y. Yang, P. Li, and Y. Huang, "Combustion characteristics in scramjet combustor operating at different inflow stagnation pressures," AIAA J. **60**(8), 4544–4565 (2022).
[34]H. B. Wang, Z. G. Wang, M. b Sun, and H. y Wu, "Nonlinear analysis of combustion oscillations in a cavity-based supersonic combustor," Sci. China Technol. Sci. **56**(5), 1093–1101 (2013).
[35]H. Lian, J. Martz, N. Prakash, and A. Stefanopoulou, "Fast computation of combustion phasing and its influence on classifying random or deterministic patterns," J. Eng. Gas Turbines Power **138**(11), 112802 (2016).
[36]G. Sugihara and R. M. May, "Nonlinear forecasting as a way of distinguishing chaos from measurement error in time series," Nature **344**(6268), 734–741 (1990).
[37]A. Krakovská, Š. Pócoš, K. MojŽišová, I. Bečková, and J. X. Gubáš, "State space reconstruction techniques and the accuracy of prediction," Commun. Nonlinear Sci. Numer. Simul. **111**, 106422 (2022).
[38]Y. Hirata, H. Suzuki, and K. Aihara, "Reconstructing state spaces from multivariate data using variable delays," Phys. Rev. E **74**(2), 026202 (2006).
[39]J. D. Farmer and J. J. Sidorowich, "Predicting chaotic time series," Phys. Rev. Lett. **59**(8), 845–848 (1987).
[40]M. Casdagli, S. Eubank, J. D. Farmer, and J. Gibson, "State space reconstruction in the presence of noise," Physica D **51**(1–3), 52–98 (1991).
[41]E. Bradley and H. Kantz, "Nonlinear time-series analysis revisited," Chaos **25**(9), 097610 (2015).
[42]A. Krakovská, K. Mezeiová, and H. Budáčová, "Use of false nearest neighbours for selecting variables and embedding parameters for state space reconstruction," J. Complex Syst. **2015**, 932750.